Construction of ZnIn 2 S 4 –In 2 O 3 hierarchical tubular heterostructures for efficient CO 2 photoreduction

Wang, Sibo; Guan, Bu Yuan; Lou, Xiong Wen David

2018

Wang, S., Guan, B. Y., & Lou, X. W. D. (2018). Construction of ZnIn 2 S 4 –In 2 O 3 Hierarchical Tubular Heterostructures for Efficient CO 2 Photoreduction . Journal of the American Chemical Society, 140(15), 5037-5040.

https://hdl.handle.net/10356/83216

https://doi.org/10.1021/jacs.8b02200

Construction of $ZnIn_2S_4$-In_2O_3 Hierarchical Tubular Heterostructures for Efficient CO_2 Photoreduction

Sibo Wang, Bu Yuan Guan, and Xiong Wen (David) Lou*

School of Chemical and Biomedical Engineering, Nanyang Technological University, 62 Nanyang Drive, Singapore 637459, Singapore

Supporting Information Placeholder

ABSTRACT: We demonstrate the rational design and construction of sandwich-like $ZnIn_2S_4$-In_2O_3 hierarchical tubular heterostructures by growing $ZnIn_2S_4$ nanosheets on both inner and outer surfaces of In_2O_3 microtubes as photocatalysts for efficient CO_2 photoreduction. The unique design integrates In_2O_3 and $ZnIn_2S_4$ into hierarchical one-dimensional (1D) open architectures with double-heterojunction shells and ultrathin two-dimensional (2D) nanosheet subunits. This design accelerates the separation and transfer of photogenerated charges, offers large surface area for CO_2 adsorption, and exposes abundant active sites for surface catalysis. Benefitting from the structural and compositional merits, the optimized $ZnIn_2S_4$-In_2O_3 photocatalyst exhibits outstanding performance for reductive CO_2 deoxygenation with considerable CO generation rate (3075 μmol h^{-1} g^{-1}) and high stability.

Solar-driven CO_2 reduction, a key process in artificial photosynthesis, has shown promise to produce carbon fuels and relieve climate change.[1] Developing efficient photocatalysts is desirable to improve CO_2 photoreduction performance for practical implementation. Due to the distinct physicochemical features, metal oxide and sulfide semiconductors together with their appropriate composites are promising photocatalysts for CO_2 conversion.[2-13] However, the achieved efficiency so far is still not satisfactory mainly because of the sluggish separation/transfer kinetics of electron-hole pairs, especially when using bulk photocatalysts.

Delicate design of heterojunction is an effective strategy to improve photocatalytic activity, owing to the rapid separation of charge carriers induced by built-in electric field.[14-16] Besides, coupling of proper semiconductors can also render enhanced photoabsorption and photostability.[11-13] Although diverse heterostructures have been developed for photocatalysis, most heterojunction photocatalysts are bulk materials with poorly controlled nanodomains of different species.[14] These conventional solid architectures still experience serious charge recombination in the bulk phase, thus limiting the photocatalytic performance.

To maximize the virtues of heterojunction for photocatalysis, the fabrication of photocatalysts with proper nanostructures is of importance. Hollow particles with unique structure-dependent merits have shown advantages in diverse research areas.[17-24] Recently, hollow architectures have been studied as photocatalysts for CO_2 reduction.[5-8] The hollow cavity not only possesses reduced bulk-to-surface diffusion length to accelerate electron-hole separation, but also provides large surface area and abundant active sites to boost CO_2 adsorption and surface catalysis.[21] Meanwhile, optical absorption could be increased by multi-light scattering/reflection in the interior void.[23] Among the various configurations of hollow scaffolds, tubular structures with two open ends may offer opportunities for hybridization with other semiconductors on both surfaces of the shell to form three-layered heterostructures. In addition, growing 2D semiconductor nanosheets on tubular substrates is favorable to reduce diffusion distance for charges and enhance exposed catalytic-active sites.[4,10] Therefore, it might be desirable to combine these considerations mentioned above and prepare novel photocatalysts to explore their benefits in CO_2 photoreduction.

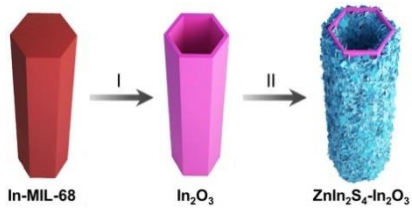

Figure 1. Schematic illustration of the synthetic process of sandwich-like $ZnIn_2S_4$-In_2O_3 hierarchical tubular heterostructures: (I) thermal annealing in air, (II) growth of $ZnIn_2S_4$ nanosheets.

Herein, we demonstrate the rational design and fabrication of sandwich-like $ZnIn_2S_4$-In_2O_3 hierarchical tubular heterostructures by assembling $ZnIn_2S_4$ nanosheets on both inner and outer surfaces of In_2O_3 microtubes as double-heterojunction photocatalysts for efficient visible-light CO_2 reduction. Figure 1 illustrates the overall synthetic processes of the complex hollow heterostructures. First, hexagonal In_2O_3 tubes are obtained through a thermal annealing treatment of In-MIL-68 prism precursor (step I).[25] Then, two layers of $ZnIn_2S_4$ nanosheets are grown on both surfaces of as-derived In_2O_3 tubes via a hydrothermal reaction (step II). The photocatalytic functions of In_2O_3 and $ZnIn_2S_4$ are integrated into hierarchical 1D hollow architectures with double-heterojunction shells and ultrathin 2D nanosheet subunits, which can assist the separation and migration of photogenerated charges, provide large surface area for CO_2 adsorption, and expose plentiful reactive sites for surface reactions. Ac-

cordingly, the optimal $ZnIn_2S_4$-In_2O_3 photocatalyst displays outstanding performance for deoxygenative CO_2 reduction with excellent CO-evolving rate (3075 μmol h^{-1} g^{-1}) and high stability.

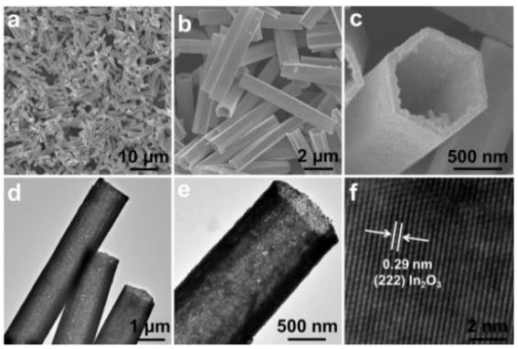

Figure 2. (a-c) FESEM images, (d,e) TEM images and (f) HRTEM image of hexagonal In_2O_3 microtubes.

Hexagonal In-MIL-68 prisms are synthesized via a solvothermal method.[26] Powder X-ray diffraction (XRD) analysis indicates the formation of In-based MIL-68 phase (Figure S1).[26] These In-MOFs present uniform hexagonal prism-shaped morphology (Figure S2). Thermogravimetric analysis (TGA) reveals In-MIL-68 can be fully converted to In_2O_3 after thermal annealing in air at 500 ˚C (Figure S3). After the treatment, cubic In_2O_3 is obtained without detectable impurities (Figure S4). Field-emission scanning electron microscopy (FESEM) images show the In_2O_3 product preserves the 1D morphology as that of In-MIL-68 prisms (Figure 2a,b). The magnified FESEM image demonstrates the well-defined hexagonal open ends of the In_2O_3 microtube (Figure 2c). The hollow feature of the In_2O_3 material is revealed by transmission electron microscopy (TEM) images (Figure 2d,e). Further TEM analysis shows the shell of In_2O_3 microtubes is assembled from small nanocrystals interconnected firmly with each other (Figure S5a,b), constructing the stable hollow structures with porous characteristics (Figure S6). In the high-resolution TEM (HRTEM) image (Figure 2f), the lattice fringes with interlayer distance of 0.29 nm are assigned to (222) crystal plane of cubic In_2O_3. The polycrystalline nature of the In_2O_3 material is indicated by selected area electron diffraction (SAED) pattern (Figure S5c). The chemical composition and distribution of the In_2O_3 microtubes are examined by energy-dispersive X-ray (EDX) spectroscopy (Figure S7) and elemental mappings (Figure S5d).

Then, two layers of ultrathin $ZnIn_2S_4$ nanosheets are grown on both inner and outer surfaces of the In_2O_3 microtubes through a low-temperature hydrothermal approach.[27] After the reaction, $ZnIn_2S_4$ nanosheets are uniformly covered on the surfaces of In_2O_3 microtubes with well-maintained overall 1D morphology and open ends (Figure 3a,b). The high-magnification FESEM images show the $ZnIn_2S_4$ layers are composed of randomly assembled nanosheets, and are grown on both surfaces of In_2O_3 microtubes (Figure 3c and Figure S8a-c), forming the sandwich-like $ZnIn_2S_4$-In_2O_3 hierarchical tubular heterostructures. XRD analysis reveals $ZnIn_2S_4$-In_2O_3 contains the mixed phases of cubic In_2O_3 and hexagonal $ZnIn_2S_4$ (Figure S9). The hierarchical hollow structure of $ZnIn_2S_4$-In_2O_3 is revealed by TEM images (Figure 3d and Figure S8d). No visible interlayer gap is found between $ZnIn_2S_4$ layers and In_2O_3 shell (Figure S8e,f), suggesting the intimate junctions between the components. FESEM and TEM characterizations for $ZnIn_2S_4$-In_2O_3 samples collected at different reaction times demonstrate the possible epitaxial growth of $ZnIn_2S_4$ nanosheets on In_2O_3 substrate (Figure S10). The heterojunction between few-layered $ZnIn_2S_4$ and In_2O_3 is revealed by HRTEM image (Figure 3e), in which the lattice fringes assigned to crystal planes of cubic In_2O_3 and hexagonal $ZnIn_2S_4$ are discerned. Besides, the two sets of diffraction fringes in SAED pattern further indicate the construction of nanosized heterojunctions between $ZnIn_2S_4$ and In_2O_3 (Figure 3f). EDX analysis determines the composition of $ZnIn_2S_4$-In_2O_3 with a $ZnIn_2S_4$ molar ratio of *ca.* 40.3 % (Figure S11). Elemental mappings of a single $ZnIn_2S_4$-In_2O_3 microtube reveal the even distribution of O, In, S and Zn (Figure 3g). Such results reflect the formation of homogeneous lengthwise interfacial junctions between In_2O_3 shell and $ZnIn_2S_4$ layers. X-ray photoelectron spectroscopy (XPS) measurements identify the valance states of elements in $ZnIn_2S_4$-In_2O_3 (Figure S12). The developed recipe is effective for modulating composition of the final heterostructures to optimize catalytic performance by controlling the amounts of $ZnIn_2S_4$ precursors. The other two samples, $ZnIn_2S_4$-In_2O_3-0.5 (half precursor amounts, Figure S13-15) and $ZnIn_2S_4$-In_2O_3-2.0 (double precursor amounts, Figure S16-18), with different compositions are synthesized. For comparison, the nanosheet-assembled $ZnIn_2S_4$ particles (Figure S19-S21) and free-standing $ZnIn_2S_4$ nanosheets ($ZnIn_2S_4$ NSs, Figure S22) are also prepared under similar conditions.[27,28]

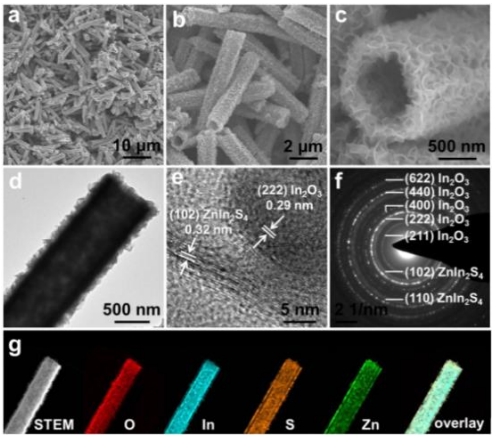

Figure 3. (a-c) FESEM images, (d) TEM image, (e) HRTEM image and (f) SAED patterns of $ZnIn_2S_4$-In_2O_3 hierarchical microtubes, and (g) EDX mappings of an individual $ZnIn_2S_4$-In_2O_3 microtube.

UV-Vis diffuse reflectance spectra (DRS) show In_2O_3 exhibits poor photoabsorption in the visible-light region. But after growth of $ZnIn_2S_4$ nanosheets, the $ZnIn_2S_4$-In_2O_3 composite displays strong visible-light absorption to ca. 500 nm (Figure S23). From the Tauc plots (Figure S24), the bandgap energies of In_2O_3, $ZnIn_2S_4$-In_2O_3 and $ZnIn_2S_4$ are calculated to be 2.73, 2.39 and 2.29 eV, respectively.[3,27] Furthermore, the conduction band (CB) positions of the materials are determined by Mott-Schottky plots (Figure S25a-c). The derived flat-band potentials of In_2O_3, $ZnIn_2S_4$-In_2O_3 and $ZnIn_2S_4$ are ca. -0.78, -0.86 and -0.98 V (*vs.* normal hydrogen electrode, NHE, pH = 7.0), which confirms their suitable redox potentials to drive CO_2 reduction reaction (Figure S25d). In addi-

tion, N_2 sorption tests reveal the porous features of $ZnIn_2S_4$-In_2O_3 with a high Brunauer-Emmett-Teller (BET) surface area of 128 $m^2\ g^{-1}$ (Figure S26), affording the material a maximum CO_2 uptake of ca. 20 $cm^3\ g^{-1}$ at 0 °C (Figure S27), which is about twice that of $ZnIn_2S_4$ particles (Figure S28). All these findings indicate the opportunity of $ZnIn_2S_4$-In_2O_3 for visible-light CO_2 reduction.

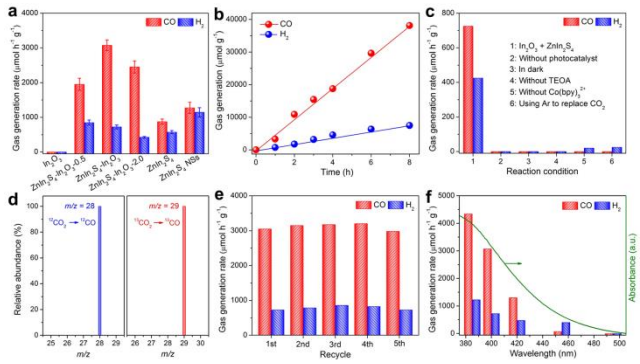

Figure 4. (a) CO_2 photoreduction activities of different samples. (b) Time-yield plots of products. (c) CO_2 reduction performance under various conditions. (d) Results of GC-MS analysis of ^{12}CO and ^{13}CO. (e) Formation of CO/H_2 in stability tests. (f) CO/H_2 production under light irradiation of different wavelengths.

Photocatalytic CO_2 reduction reactions are conducted in H_2O/acetonitrile mixture with $Co(bpy)_3^{2+}$ (bpy = 2'2-bipyridine) and triethanolamine (TEOA) as the cocatalyst and electron donor, respectively.[29] Bare In_2O_3 is inactive to reduce CO_2 under visible-light irradiation (Figure 4a); while the $ZnIn_2S_4$ particles and $ZnIn_2S_4$ NSs enable the deoxygenative CO_2 reduction with CO-evolving rates of 875 and 1275 μmol $h^{-1}\ g^{-1}$, respectively. However, the three heterojunction photocatalysts manifest enhanced CO_2-to-CO conversion activities. Strikingly, the $ZnIn_2S_4$-In_2O_3 sample displays the highest CO evolution rate of 3075 μmol $h^{-1}\ g^{-1}$. This CO_2 reduction rate is comparable to that of many other CO_2 conversion systems (Table S1). Moreover, $ZnIn_2S_4$-In_2O_3 also exhibits durable CO_2 reduction activity during photoreaction for 8 h (Figure 4b), affording an accumulated product yield of ca. 4.56×10^4 μmol g^{-1}. These results underline the remarkable CO_2 reduction performance of $ZnIn_2S_4$-In_2O_3, which should be related to the unique structures and compositions of the three-layered hierarchical tubular heterostructures for boosting the separation and transfer of photoexcited charges.

Control experiments demonstrate the CO_2 reduction performance of a physical mixture of In_2O_3 and $ZnIn_2S_4$ is much inferior to that of $ZnIn_2S_4$-In_2O_3 (Figure 4c, column 1), indicating the importance of intimate interfacial contact and strong interactions in the heterostructures for the reaction. Besides, if the CO_2 reduction reaction is performed without photocatalyst or light irradiation, no CO/H_2 can be detected (Figure 4c, column 2 and column 3), suggesting photocatalytic nature of the reaction. Meanwhile, no obvious CO_2-to-CO conversion reaction is observed without TEOA or $Co(bpy)_3^{2+}$ (Figure 4c, column 4 and column 5).[30] In addition, when using Ar as the reaction gas, there is not any CO evolution detected (Figure 4c, column 6). This result indicates the CO product originates from splitting of CO_2 molecules, which is further verified by $^{13}CO_2$ isotope experiment. Only ^{13}CO is detected when reaction is operated in a $^{13}CO_2$ atmosphere (Figure 4d), confirming CO_2 is the carbon source of CO formation. To evaluate stability, $ZnIn_2S_4$-In_2O_3 is repeatedly employed to run the CO_2 reduction reaction for 5 cycles. No obvious deactivation is observed during the tests (Figure 4e), highlighting the high stability of $ZnIn_2S_4$-In_2O_3. Besides, XRD and FESEM tests of used $ZnIn_2S_4$-In_2O_3 after photocatalysis also support the stability of the catalyst (Figure S29). Wavelength-dependent CO_2 reduction reactions are conducted on $ZnIn_2S_4$-In_2O_3. The trend of CO/H_2 evolution matches well with photoabsorption of the heterojunction photocatalyst (Figure 4f), indicating the CO_2 reduction reaction is induced by photoexcitation of $ZnIn_2S_4$-In_2O_3.[30]

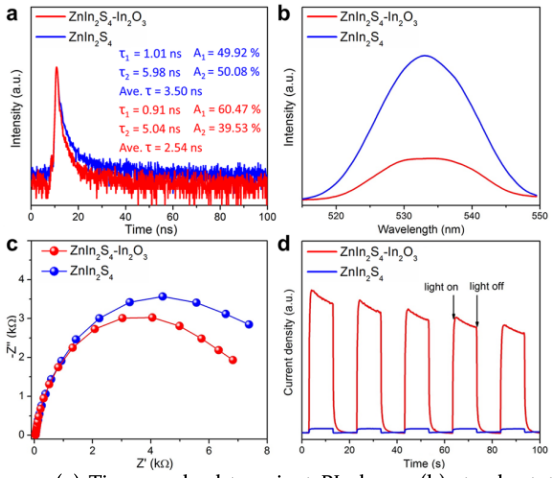

Figure 5. (a) Time-resolved transient PL decay, (b) steady-state PL spectra, (c) EIS spectra, and (d) transient photocurrent spectra of $ZnIn_2S_4$-In_2O_3 and $ZnIn_2S_4$.

Photoelectrochemical characterizations are performed to elucidate the high CO_2 reduction performance of $ZnIn_2S_4$-In_2O_3 heterojunction photocatalyst. First, the specific charge carrier dynamics of $ZnIn_2S_4$-In_2O_3 and $ZnIn_2S_4$ particles are probed by time-resolved photoluminescence (PL) spectroscopy (Figure 5a). The average emission lifetime of $ZnIn_2S_4$-In_2O_3 (2.54 ns) is shorter than that of $ZnIn_2S_4$ (3.50 ns). Meanwhile, steady-state PL spectra show the significant PL quenching of the heterostructures (Figure 5b). The obvious PL quenching and lifetime decrease indicate the formation of an electron transfer pathway from $ZnIn_2S_4$ to In_2O_3 in a non-radiative quenching manner.[9] Therefore, efficient interfacial charge migration and separation are achieved in $ZnIn_2S_4$-In_2O_3. On the other hand, electrochemical impedance spectra (EIS) reveal $ZnIn_2S_4$-In_2O_3 manifests a smaller semicircular in Nyquist plots (Figure 5c), suggesting a lower charge-transfer resistance in the heterostructures that permits fast transport and separation of photoinduced charges. Moreover, transient photocurrent spectra indicate $ZnIn_2S_4$-In_2O_3 exhibits a greatly enhanced photocurrent than $ZnIn_2S_4$ particles (Figure 5d), revealing the promoted generation and transfer of photogenerated electron-hole pairs in the heterostructures. All these observations demonstrate the $ZnIn_2S_4$-In_2O_3 hierarchical hollow photocatalyst can enhance the generation, separation and transport of photoinduced charges, thus rendering high-efficiency of CO_2 photoreduction.

In summary, sandwich-like $ZnIn_2S_4$-In_2O_3 hierarchical tubular heterostructures are designed and assembled by growing $ZnIn_2S_4$ nanosheets on both inner and outer surfaces

of In_2O_3 microtubes as double-heterojunction photocatalysts for efficient visible-light CO_2 reduction. The facile synthetic strategy, involving a thermal annealing treatment and a low-temperature hydrothermal reaction, can control the structures and compositions of the final heterostructures. These complex hollow scaffolds featuring dual interfacial heterojunction shells and ultrathin 2D nanosheet subunits remarkably promote the separation and transfer of photogenerated charge carriers, deliver large surface area for CO_2 adsorption, and expose rich active sites for surface catalysis. As a result, the optimal $ZnIn_2S_4$-In_2O_3 photocatalyst shows outstanding performance for deoxygenative CO_2 reduction with considerable CO evolution rate (3075 μmol h^{-1} g^{-1}) and high stability. This work may inspire the development of complex hollow photosynthetic assemblies for artificial photosynthesis.

ASSOCIATED CONTENT

Supporting Information

The experimental details, more FESEM/TEM images, XRD, EDX, DRS, Tauc plots, Mott-Schottky plots, N_2 adsorption isotherms, CO_2 sorption isotherms. This material is available free of charge via the Internet at http://pubs.acs.org.

AUTHOR INFORMATION

Corresponding Author

Email: xwlou@ntu.edu.sg

Notes

The authors declare no competing financial interests.

ACKNOWLEDGEMENTS

X. W. L. acknowledges the funding support from the National Research Foundation (NRF) of Singapore via the NRF investigatorship (NRF-NRFI2016-04).

REFERENCES

(1) Listorti, A.; Durrant, J.; Barber, J. *Nat. Mater.* **2009**, *8,* 929.
(2) Pan, Y. X.; You, Y.; Xin, S.; Li, Y.; Fu, G.; Cui, Z.; Men, Y. L.; Cao, F. F.; Yu, S. H.; Goodenough, J. B. *J. Am. Chem. Soc.* **2017**, *139*, 4123.
(3) Hoch, L. B.; Wood, T. E.; O'Brien, P. G.; Liao, K.; Reyes, L. M.; Mims, C. A.; Ozin, G. A. *Adv. Sci.* **2014**, *1*, 1400013.
(4) Gao, S.; Gu, B.; Jiao, X.; Sun, Y.; Zu, X.; Yang, F.; Zhu, W.; Wang, C.; Feng, Z.; Ye, B.; Xie, Y. *J. Am. Chem. Soc.* **2017**, *139*, 3438.
(5) In, S. I.; Vaughn, D. D.; Schaak, R. E. *Angew. Chem. Int. Ed.* **2012**, *51*, 3915.
(6) Wang, S.; Guan, B. Y.; Lou, X. W. *Energy Environ. Sci.* **2018**, 11, 306.
(7) Tu, W.; Zhou, Y.; Liu, Q.; Tian, Z.; Gao, J.; Chen, X.; Zhang, H.; Liu, J.; Zou, Z. *Adv. Funct. Mater.* **2012**, *22*, 1215.
(8) Wang, S.; Guan, B. Y.; Lu, Y.; Lou, X. W. *J. Am. Chem. Soc.* **2017**, *139*, 17305.
(9) Yang, M. Q.; Xu, Y. J.; Lu, W.; Zeng, K.; Zhu, H.; Xu, Q. H.; Ho, G. W. *Nat. Commun.* **2017**, *8*, 14224.
(10) Jiao, X.; Chen, Z.; Li, X.; Sun, Y.; Gao, S.; Yan, W.; Wang, C.; Zhang, Q.; Lin, Y.; Luo, Y.; Xie, Y. *J. Am. Chem. Soc.* **2017**, *139*, 7586.
(11) Jiao, X.; Li, X.; Jin, X.; Sun, Y.; Xu, J.; Liang, L.; Ju, H.; Zhu, J.; Pan, Y.; Yan, W.; Lin, Y.; Xie, Y. *J. Am. Chem. Soc.* **2017**, *139*, 18044.
(12) Iwase, A.; Yoshino, S.; Takayama, T.; Ng, Y. H.; Amal, R.; Kudo, A. *J. Am. Chem. Soc.* **2016**, *138*, 10260.
(13) Wakerley, D. W.; Kuehnel, M. F.; Orchard, K. L.; Ly, K. H.; Rosser, T. E.; Reisner, E. *Nat. Energy* **2017**, *2*, 17021.
(14) Wang, H.; Zhang, L.; Chen, Z.; Hu, J.; Li, S.; Wang, Z.; Liu, J.; Wang, X. *Chem. Soc. Rev.* **2014**, *43*, 5234.
(15) Kuriki, R.; Matsunaga, H.; Nakashima, T.; Wada, K.; Yamakata, A.; Ishitani, O.; Maeda, K. *J. Am. Chem. Soc.* **2016**, *138*, 5159.
(16) Kuriki, R.; Yamamoto, M.; Higuchi, K.; Yamamoto, Y.; Akatsuka, M.; Lu, D.; Yagi, S.; Yoshida, T.; Ishitani, O.; Maeda, K. *Angew. Chem. Int. Ed.* **2017**, *56*, 4867.
(17) Guan, B. Y.; Yu, X. Y.; Wu, H. B.; Lou, X. W. *Adv. Mater.* **2017**, *29*, 1703614.
(18) Wang, S.; Guan, B. Y.; Yu, L.; Lou, X. W. *Adv. Mater.* **2017**, *29*, 1702724.
(19) Guan, B. Y.; Yu, L.; Li, J.; Lou, X. W. *Sci. Adv.* **2016**, *2*, e1501554.
(20) Yu, L.; Wu, H. B.; Lou, X. W. *Acc. Chem. Res.* **2017**, *50*, 293.
(21) Zheng, D.; Cao, X. N.; Wang, X. *Angew. Chem. Int. Ed.* **2016**, *55*, 11512.
(22) Qiu, B.; Zhu, Q.; Du, M.; Fan, L.; Xing, M.; Zhang, J. *Angew. Chem. Int. Ed.* **2017**, *56*, 2684.
(23) Sun, J.; Zhang, J.; Zhang, M.; Antonietti, M.; Fu, X.; Wang, X. *Nat. Commun.* **2012**, *3*, 1139.
(24) Zhang, P.; Guan, B. Y.; Yu, L.; Lou, X. W. *Chem* **2018**, *4*, 162.
(25) Zhang, H.; Nai, J.; Yu, L.; Lou, X. W. *Joule* **2017**, *1*, 77.
(26) Cho, W.; Lee, H. J.; Oh, M. *J. Am. Chem. Soc.* **2008**, *130*, 16943.
(27) Chen, Z.; Li, D.; Zhang, W.; Chen, C.; Li, W.; Sun, M.; He, Y.; Fu, X. *Inorg. Chem.* **2008**, *47*, 9766.
(28) Yang, W.; Zhang, L.; Xie, J.; Zhang, X.; Liu, Q.; Yao, T.; Wei, S.; Zhang, Q.; Xie, Y. *Angew. Chem. Int. Ed.* **2016**, *55*, 6716.
(29) Zheng, Y.; Lin, L.; Ye, X.; Guo, F.; Wang, X. *Angew. Chem. Int. Ed.* **2014**, *53*, 11926.
(30) Qin, J.; Wang, S.; Ren, H.; Hou, Y.; Wang, X. *Appl. Catal. B: Environ.* **2015**, *179*, 1.

TOC graphic

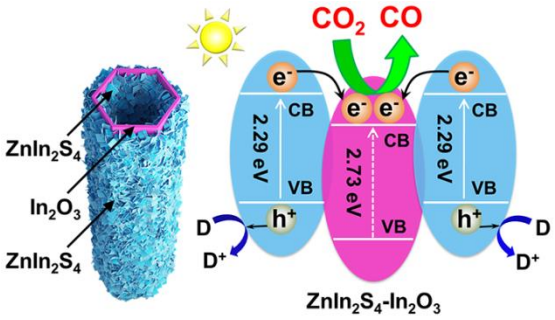
CO2 CO
e-
e-
e-
e-
CB
CB
CB
2.29 eV
2.73 eV
2.29 eV
VB
VB
VB
h+
h+
D
D+
D
D+
ZnIn2S4
In2O3
ZnIn2S4
ZnIn2S4-In2O3